metals

MDPI

Article

Effect of Rotational Speed on Mechanical Properties of AA5083/AA6082 Friction Stir Welded T-Joints for Naval Applications

Guido Di Bella [1,*], Chiara Borsellino [1], Mohamed Chairi [1], Davide Campanella [2] and Gianluca Buffa [2]

[1] Department of Engineering, University of Messina, 98166 Messina, Italy; chiara.borsellino@unime.it (C.B.); mohamed.chairi@unime.it (M.C.)
[2] Department of Engineering, University of Palermo, 90128 Palermo, Italy; davide.campanella@unipa.it (D.C.); gianluca.buffa@unipa.it (G.B.)
* Correspondence: guido.dibella@unime.it; Tel.: +39-090-6765310

Abstract: This study evaluates the influence of rotational speed on the mechanical and microstructural properties of T-joints fabricated via friction stir welding (FSW) using dissimilar aluminum alloys, AA5083 and AA6082, for naval applications. Three types of joints were produced by maintaining a constant traverse speed of 100 mm/min and varying the tool rotational speed at 500, 700, and 900 rpm. Mechanical performance was assessed through pull-out tests and microhardness measurements. The joints fabricated at 500 rpm demonstrated superior mechanical properties, including a more uniform hardness distribution and higher pull-out strength, attributed to optimized material mixing and heat input at this speed. In contrast, higher rotational speeds led to defect formation, such as wormholes, and compromised mechanical performance. These findings underscore the importance of optimizing rotational speed to enhance joint quality, making FSW a viable solution for manufacturing durable, lightweight structures in demanding marine environments.

Keywords: friction stir welding; joining; aluminum; shipbuilding; manufacturing

Citation: Di Bella, G.; Borsellino, C.; Chairi, M.; Campanella, D.; Buffa, G. Effect of Rotational Speed on Mechanical Properties of AA5083/AA6082 Friction Stir Welded T-Joints for Naval Applications. *Metals* **2024**, *14*, 1410. https://doi.org/10.3390/met14121410

Academic Editors: Masahiro Fukumoto and John D. Clayton

Received: 15 November 2024
Revised: 30 November 2024
Accepted: 7 December 2024
Published: 10 December 2024

1. Introduction

Friction stir welding (FSW) has emerged as a pivotal technique across diverse industrial sectors, including automotive, aerospace, and marine industries, where lightweight and robust structures are indispensable [1,2]. As a solid-state joining process, FSW eliminates the melting phase, thus minimizing thermal distortion, residual stresses, and defects typically associated with conventional fusion welding techniques [3,4]. This unique capability makes FSW particularly suited for high-performance applications, especially in environments demanding corrosion resistance and structural integrity [5]. Initially developed for joining similar materials in simple butt joint configurations, FSW has evolved to accommodate dissimilar material combinations and complex joint geometries [6]. This adaptability is critical for marine applications, where aluminum alloys are widely used due to their low density, excellent corrosion resistance, and favorable mechanical properties [7].

The capacity of FSW to join dissimilar materials [8], such as various aluminum alloys [9] or even aluminum with steel [10,11], presents significant strategic advantages. Aluminum alloys, widely used in marine applications for their low density, high corrosion resistance, and favorable mechanical properties [12,13], benefit from FSW precision in joining without sacrificing the structural integrity of either material. Welding dissimilar aluminum alloys, for example, allows to leverage the specific properties of each alloy within a single structural component [14]. This adaptability can enhance the performance of naval structures, enabling designs that are both lighter and more resistant to environmental stressors. The FSW process thus supports the integration of high-strength components while maintaining a balance between weight efficiency and structural robustness.

Nor and Shazarel [15] apply FSW process to join aluminum alloys AA6061-T6 and AA5083-H116 in butt joint configurations with specimens used for marine applications. Key parameters are adjusted, including material thickness (3 mm, 4 mm, and 5 mm), rotational speed (800, 1200, and 1600 rpm), feed rate (30, 60, and 90 mm/min), pin length (92.5%, 95%, and 97.5% of material thickness), and dwell time (15, 20, and 25 min). The optimization of tensile strength and hardness responses is conducted using Response Surface Methodology (RSM). Osorio et al. [16] identify a process window to improve mechanical properties and reduce discontinuities in dissimilar friction stir welded joints of AA6063-T6 and AA5052-H32 alloys. By testing various rotational and traverse speeds, and analyzing microstructure through optical microscopy, X-ray diffraction, and SEM-EDS, they find that a speed ratio of 1800 rpm/163 mm/min yields high-quality joints with increased microhardness and a tensile strength of 159 MPa. Verma and Kumar [17] use FSW to join AA6061-T6 and AA5083-O plates, examining how tool pin profile, rotation speed, feed rate, and tilt angle impact tensile strength and elongation. Using Box–Behnken design and regression models, they find that strength and elongation increase with welding parameters up to an optimal point before declining. The straight cylindrical (SC) pin profile produces the highest strength (135.83 MPa) and elongation (4.35%) at 1568 rpm, 39.53 mm/min feed rate, and 1.11° tilt angle.

In addition to joining dissimilar materials, FSW accommodates various joint configurations, expanding its applicability to complex geometries such as T-joints [18]. The T-joint, commonly used in marine frameworks to connect perpendicular components, is essential in constructing durable and stable structures. However, T-joints pose specific challenges in FSW due to their geometry and the need for controlled heat distribution and material flow to produce a high-quality weld. Achieving defect-free joints in such configurations requires precise control over FSW parameters. Key process parameters—including tool rotational speed, travel speed, axial force, and tool tilt angle—directly impact the heat generation, material flow, and ultimate quality of the joint. Of these, the tool rotational speed plays a critical role, as it influences both the temperature and the degree of material mixing around the tool, affecting the weld's microstructure, mechanical properties, and defect susceptibility. Inadequate or excessive rotational speeds may lead to incomplete mixing, void formation, or undesirable softening, thereby compromising joint strength and fatigue resistance.

Tavares et al. [19] explore FSW T-joints of dissimilar aluminum alloys, ideal for reinforced panels where a tougher skin alloy and a stronger web alloy provide a damage-tolerant design. The proposed T-joint configuration excludes overlap interfaces, allowing effective material flow for robust welds. Mechanical tests show high static and dynamic strength but reduced elongation. Microstructural analysis of the weld zone, compared to base materials and butt joints, confirms the feasibility of joining dissimilar aluminum alloys in T-joints. Jesus et al. [20] weld AA 5083-H111 and AA 6082-T6 plates in T-butt and T-lap configurations using three tool pin geometries: tapered/threaded, quadrangular pyramidal, and progressive pin. Welds with a pyramidal pin show tunnel defects, kissing bonds, and oxide lines, while tapered pin welds only have kissing-bond defects. The progressive pin welds are defect-free. Hardness remains consistent across tools and joint types, but the progressive pin in the T-butt configuration yields the best mechanical performance, with T-butt joints outperforming T-lap joints in FSW. Sabry et al. [21] successfully produce T-joints of AA6063-T6 using FSW and a specially developed fixture, resulting in defect-free welds. They analyze the effects of tool rotation speed, axial force, and travel speed on tensile strength, hardness in various zones (thermal, heat-affected, and nugget), and temperature distribution. Rana et al. [22] examine FSW for joining highly dissimilar materials, specifically aluminum alloy 6156 and commercially pure Ti grade 2, using both numerical simulation and experimental validation. The research highlights the need for balanced parameters to achieve appropriate heat flux, influencing material flow and properties. A numerical model predicts field variables and material flow in Al–Ti skin–stringer joints, with findings on material flow changes based on skin-stringer positioning. Macrostructural

and microstructural analyses reveal insights into grain refinement, intermetallic formation, and defects. Results show that joint strength in T-joints is comparable to butt joints reported in the literature.

Recent advancements in welding process optimization have integrated numerical simulations, artificial intelligence (AI), and Internet of Things (IoT) technologies to enhance joint quality and process efficiency. These methods enable precise control and prediction of welding outcomes, particularly in complex configurations like T-joints. Memon et al. [23] investigated the effects of friction stir welding (FSW) tool offset on the mixing and bonding of Al–Mg–Si alloys in T-configurations. Using computational fluid dynamics (CFD) simulations, they demonstrated that an appropriate tool offset is crucial for optimal material flow and joint integrity. Specifically, a +0.2 mm offset on the advancing side resulted in the most robust joint, retaining over 60% of the base aluminum alloy's strength. Similarly, Salloomi [24] conducted a fully coupled thermomechanical simulation of the FSW process for aluminum 6061–T6 alloy T-joints. The study evaluated temperature distribution, stress, strain, tool reaction forces, and energy dissipation during the welding phases. The simulation results showed symmetrical temperature distribution across the T-joint width, with a high gradient in the weld stirring zone after the plunge stage. Experimental validation using embedded thermocouples confirmed the numerical findings, indicating good correlation with minimal deviation in peak values. Additionally, Silva et al. [25] focused on optimizing FSW T-joints using the Taguchi method. Mechanical testing of 27 different welded joints revealed that tool rotational speed significantly influences joint mechanical properties and is strongly dependent on the shoulder/probe diameter ratio. The study identified that a rotational speed of 1000 rpm, a probe depth of 3.90 mm, and a shoulder/probe diameter ratio of 2.5 (with a shoulder diameter of 15 mm) yielded improved joint strength. Notably, under these optimized parameters, welding speed did not significantly affect the outcomes. These studies underscore the importance of precise parameter optimization in FSW of T-joints to achieve superior mechanical properties and joint integrity.

This study examines the effect of rotational speed [26] on the mechanical properties of T-joints fabricated via FSW from dissimilar aluminum alloys, AA5083 and AA6082, specifically for naval applications. The research focuses on how variations in rotational speed influence the formation of weld imperfections, such as wormholes, and the overall mechanical performance of the joints. By investigating these aspects, the study aims to establish a clear understanding of the relationship between process parameters and joint quality. The primary objective is to optimize FSW process settings to achieve high-quality, durable joints that balance mechanical performance and weight reduction, addressing the stringent demands of marine environments. Particularly, joining aluminum alloys AA5083 and AA6082 offers a balanced combination of properties ideal for demanding applications. AA5083 provides excellent corrosion resistance, particularly in marine environments, while AA6082 contributes higher mechanical strength. This synergy creates a lightweight, durable joint that is well-suited for structural applications in marine, automotive, and aerospace industries. Additionally, combining these alloys can be more cost-effective than using alternative materials, offering enhanced fatigue performance and versatility across various high-performance applications.

For the study in question, three different levels of heat input were considered. Specifically, with a constant tool feed rate of 100 mm/min, the tool rotational speed was varied from 500 rpm to 900 rpm, with an intermediate step at 700 rpm. Mechanical evaluation, including pull-out tests and microhardness measurements, was performed to assess the performance of each joint type. The results indicate that T-joints produced in transparency modality at a rotational speed of 500 rpm exhibited enhanced mechanical properties, including higher pull-out strength and a stable hardness distribution. This study demonstrates that selecting a rotational speed of 500 rpm, which balances heat input, material mixing, and defect minimization, significantly improves the mechanical quality and robustness of T-joints. The results presented are the averages of three independent tests for each welding condition, with standard deviations calculated to evaluate data variability. Fracture surface

analyses confirmed the presence of characteristic defects, such as wormholes, particularly at higher rotational speeds, which correlate with decreased mechanical performance. These findings were consistent across samples, supporting the robustness of the conclusions drawn. These findings highlight the potential of FSW for creating durable, lightweight structures that meet the stringent demands of the marine industry.

2. Materials and Methods

2.1. Materials

The T-joint setup for this study employs two aluminum alloys, i.e., AA6082 and AA5083, both with a thickness of 6 mm. The sizes are, respectively, 100 mm × 70 mm and 100 mm × 50 mm. The skin component is fabricated from AA6082, an aluminum–silicon–magnesium–manganese alloy from the 6000 series, known for its versatile use in general applications. AA6082 offers high mechanical strength, positioned among the highest in its series, with good corrosion resistance, excellent weldability, and machinability, making it suitable for sheets, plates, bars, tubes, and profiles. It is typically available in the T6 temper, with other tempers upon request. This alloy is frequently used in automotive and rail construction, as well as in structural and architectural components where high corrosion resistance is a key requirement. The stringer is constructed from AA5083, an aluminum–magnesium alloy valued for its outstanding oxidation and corrosion resistance, though with moderate mechanical strength and good formability. AA5083 is also weldable by fusion and retains high toughness at both ambient and low temperatures. This alloy is commonly available in the 0/H111 temper for maximum formability and in the H22 temper, which balances formability with increased strength. AA5083 finds wide application in marine and cryogenic structures, pressure vessels, tankers, panels, wheels, and other components requiring fatigue resistance and good durability in corrosive environments without the need for high static mechanical strength. It is a suitable choice for components to be integrated into welded assemblies.

Tables 1 and 2 show the chemical composition and the main mechanical properties of the two alloys. The metallurgical characteristics of AA5083 and AA6082 play a pivotal role in their behavior during friction stir welding (FSW), particularly in dissimilar joint configurations. AA5083, classified as a strain-hardenable aluminum–magnesium alloy, derives its strength primarily from solid solution strengthening and strain hardening. Its high magnesium content enhances corrosion resistance, especially in marine environments, while contributing to moderate mechanical strength. However, its non-heat-treatable nature limits further strength enhancement through thermal treatments, making it sensitive to the heat input during FSW. Excessive heat can result in a loss of strain hardening effects, leading to localized softening. Conversely, AA6082, a precipitation-hardenable alloy from the 6000 series, relies on the formation of Mg_2Si precipitates for its strength, particularly in the T6 temper. During FSW, the thermal cycle can dissolve these precipitates and induce grain growth in the Weld Zone (WZ) and adjacent areas, such as the Heat-Affected Zone (HAZ). These changes can reduce mechanical performance, necessitating precise control of the heat input to preserve the alloy's properties. The combination of these two alloys in dissimilar FSW joints introduces additional complexities. Studies have shown that process parameters, particularly rotational speed and tool feed rate, significantly influence the joint's mechanical properties and microstructure. Higher rotational speeds tend to enhance material mixing and interfacial bonding but can also lead to defects such as voids or wormholes due to turbulent flow. On the other hand, lower rotational speeds reduce the risk of defect formation but may limit effective mixing, especially in the Stir Zone (SZ), where both alloys interface. Residual stress formation is another critical factor in dissimilar joints of AA5083 and AA6082. AA5083, being softer, accommodates more deformation, resulting in an asymmetric distribution of residual stresses. This asymmetry affects the overall mechanical performance and fatigue resistance of the joint. Optimizing FSW parameters for these alloys involves balancing heat input to achieve effective mixing, minimize defects, and maintain the inherent mechanical properties of both materials. A

moderate rotational speed can help create a homogeneous weld zone and ensure a smooth transition between the two base materials, which is essential for applications requiring robust and reliable joints [27,28].

Table 1. Chemical composition of AA6082 and AA5083 alloys (weight %).

	Al	Cr	Cu	Fe	Mg	Mn	Si	Ti	Zn	Others
AA6082	95.20–98.30	<0.25	<0.1	<0.5	0.6–1.2	0.4–1.0	0.7–1.3	0.10	0.20	0.15
AA5083	92.55–95.55	0.05–0.25	<0.1	<0.4	4.0–4.9	0.4–1.0	<0.4	0.15	0.25	-

Table 2. Mechanical properties of AA6082 and AA5083 alloys.

	Rm [MPa]	$Rp_{0.2}$ [MPa]	A [%]	HB
AA6082	310	260	10	94
AA5083	275	125	15	75

2.2. Joining Manufacturing

The joints were produced in accordance with [18], under controlled laboratory conditions, with standard temperature and humidity levels, ensuring consistency in the welding environment, using a 3-axis ESAB LEGIO™ 3ST FSW machine (OEMER Motori Elettrici, Rescaldina, Italy—Figure 1a), where the aluminum plates (i.e., skin and stringer) were fixed with a clamping device (see Figure 1b) [29]. This equipment, similar in structure to a manual milling machine, benefits from force-controlled operation in addition to positional control, enhancing the precision of the friction stir welding (FSW) process. The machine operates under a PLC (Programmable Logic Controller) interface, which provides real-time control and data recording for variables such as applied force, spindle resistance torque, displacement along the *z* and *x* axes, spindle current, and spindle power.

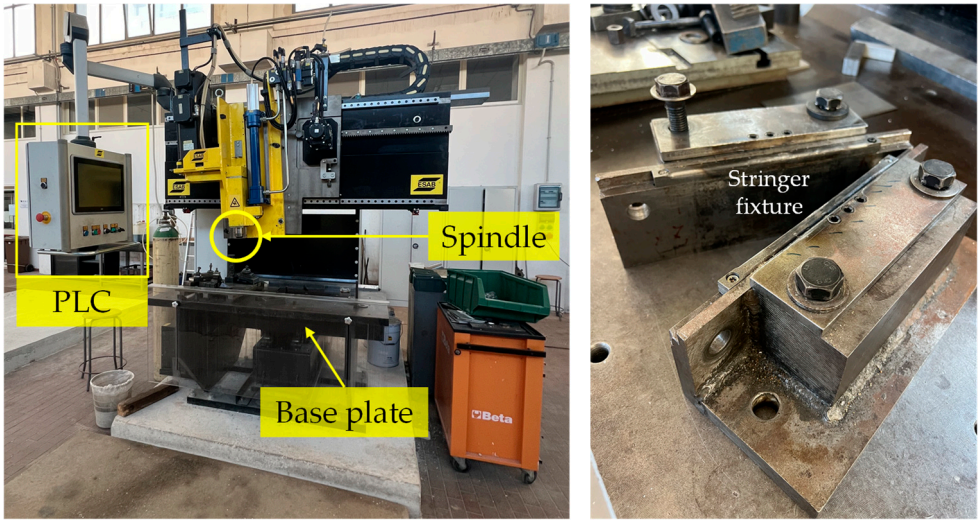

(**a**) (**b**)

Figure 1. (**a**) FSW machine. (**b**) Clamping device.

To ensure robust weld quality, a double-shoulder tool design was used (see Figure 2), particularly beneficial in T-joint configurations to enhance heat distribution at the tool edges and reduce the risk of tunnel defects. This design mitigates common issues in transparency-welded T-joints, where excessive heat generated by the shoulder on the skin can cause an uneven heat spread, forming a comet-like expansion pattern on the skin. The double-shoulder approach enables focused heat transfer, allowing the weld to forge effectively at

the intersections with the skin and stringer, leading to well-forged connections. The tool was made of H13 tool steel, selected for its high wear resistance and thermal stability, with a hardness of approximately 50 HRC.

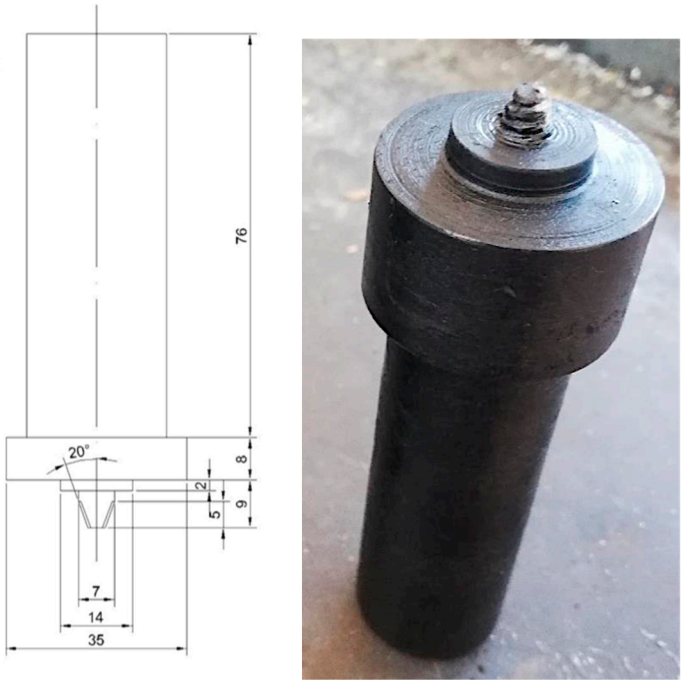

Figure 2. Schematic representation of the tool used for FSW. All dimensions are in millimeters.

For this study, three distinct heat input levels (low, medium, and high) were tested to observe variations in joint quality. Then, the welding parameters included three rotational speeds (900 rpm, 700 rpm, and 500 rpm) at a welding speed of 100 mm/min. These rotational speeds were selected to represent a range of heat inputs, allowing the investigation of their influence on defect formation, material mixing, and mechanical performance. The experimental setup ensured a stable welding process with well-defined steady-state regions, enabling a thorough analysis of the mechanical properties.

Figure 3 shows a typical sample after the FSW process. For each configuration, three of these were manufactured. It is possible to observe:

- in the top view, the forging intersections between the skin and the stringer;
- in the bottom view, both the welding area with the points of start and end and the directions of advancing and retreating.

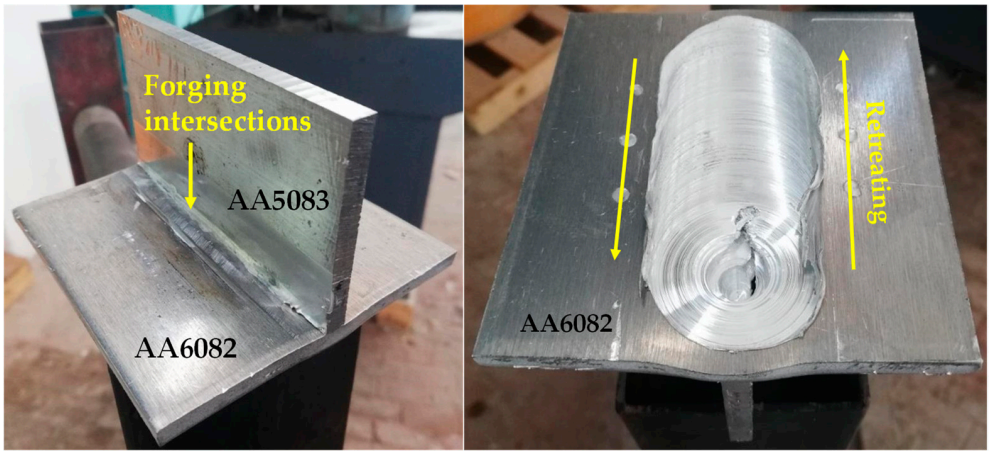

Figure 3. Friction stir welded T-joint (top and bottom view).

2.3. Testing

The experimental testing in this study was solely conducted on the friction stir welded T-joints, without performing additional tests on the base materials. This approach aligns with the study's primary objective of evaluating the joint performance and understanding the effects of rotational speed on weld quality and mechanical behavior.

2.3.1. Pull-Out Tests

A Zwick-Roell 600 Universal Testing Machine (ZwickRoell S.r.l., Genova, Italy), equipped with a 10 kN load cell and tension clamps, was used to evaluate the pull-out resistance of the T-joints, following the procedure described in [18]. Figure 4 illustrates the test scheme by identifying all parts of the clamping apparatus. The clamping plates are manufactured to avoid in the contact area with the sample each stress concentration that can induce premature failures.

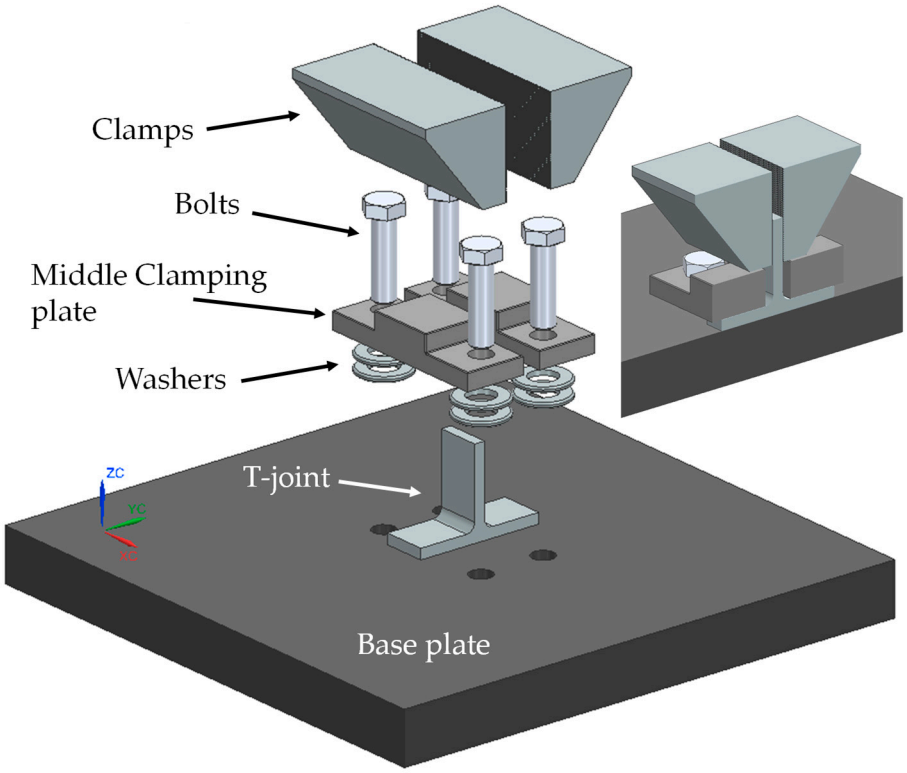

Figure 4. Pull-out tensile test scheme with the identification of all parts.

To ensure the reliability of the results, all tests were conducted on at least three samples for each welding condition. Samples with a standardized width of 25 mm were extracted from the central regions of the welded joints to minimize variability and ensure representativeness. Additionally, the pull-out tests were performed under controlled conditions, using calibrated equipment to guarantee consistent loading rates (i.e., 2 mm/min) and measurement accuracy.

The pull-out test offers distinct advantages over conventional tensile tests when evaluating T-joints. Unlike tensile testing, which applies a purely axial force, the pull-out test more accurately simulates real-world loading conditions by focusing on the resistance of a joint against detachment forces. This approach can provide insights into the adhesion strength, failure mechanisms, and quality of the bond between materials, especially important in assessing joints with complex geometries or varying cross-sectional properties. Additionally, pull-out tests can better reveal weak points across different weld zones, such as the Heat-Affected Zone (HAZ) or the Thermo-Mechanically Affected Zone (TMAZ), which are critical for understanding performance under operational stresses.

Fracture surfaces were examined to validate the observed failure modes and identify potential defects, such as wormholes.

2.3.2. Micro-Hardness

The joint was sectioned to prepare a sample that is representative of the stable length of weld. Its surface was first polished using sandpapers with grit sizes from 500 to 2000 to achieve a mirror-like surface finish before performing the microhardness tests on cross sections extracted from the center of the welds. Specifically, Vickers hardness tests were performed using a FUTURE-TECH FM-300e (FUTURE TECH CORP., Kawasaki City, Japan) microhardness tester, applying a 200 g load. In accordance with ASTM E384-17 Standard [30], the spacing between adjacent indentations was maintained at a minimum of 2.5 times the diagonal length of each indentation to prevent any interference between measurements. The tests were conducted with a dwell time of 15 s under a load of 200 g. These measurements provide valuable insights into the hardness distribution across the weld zones, helping to assess the effects of friction stir welding on material properties. Hardness variations across different zones, such as the Stir Zone (SZ), Thermo-Mechanically Affected Zone (TMAZ), and Heat-Affected Zone (HAZ), can reveal important information about the microstructural transformations induced by the welding process [31].

Figure 5a reports the test plan for the direction along the skin. The measurements were conducted along three parallel lines: upper, middle, and lower, including about 44 measurements for each line. Figure 5b reports the test plan for the direction along the stringer at the interface between the two alloys. The measurements were conducted along three parallel lines: left, middle, and right, including about 23 measurements for each sample.

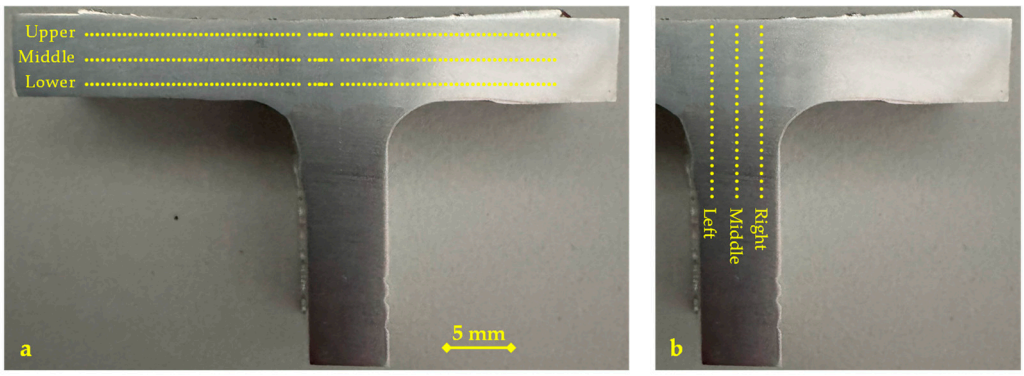

Figure 5. Test plan: (**a**) along the kin direction; (**b**) along the stringer direction.

3. Results and Discussion

Joints produced at different rotational speeds exhibited notable visual differences. At 500 rpm, the joint surface appeared smooth and defect-free, while at higher speeds (700 rpm and 900 rpm), surface irregularities and indications of wormhole defects were more prominent. These observations align with the mechanical and microstructural analyses discussed in this study.

3.1. Pull-Out Tests

To understand the junction mechanical performance of the specimens, T-pull tests were chosen as the first analysis. Figure 6 shows the load-displacement curve for the sample welded at 500 rpm, accompanied by sequential images illustrating the fracture evolution at corresponding points along the curve. This comprehensive representation elucidates the material behavior under load and the progression of failure mechanisms.

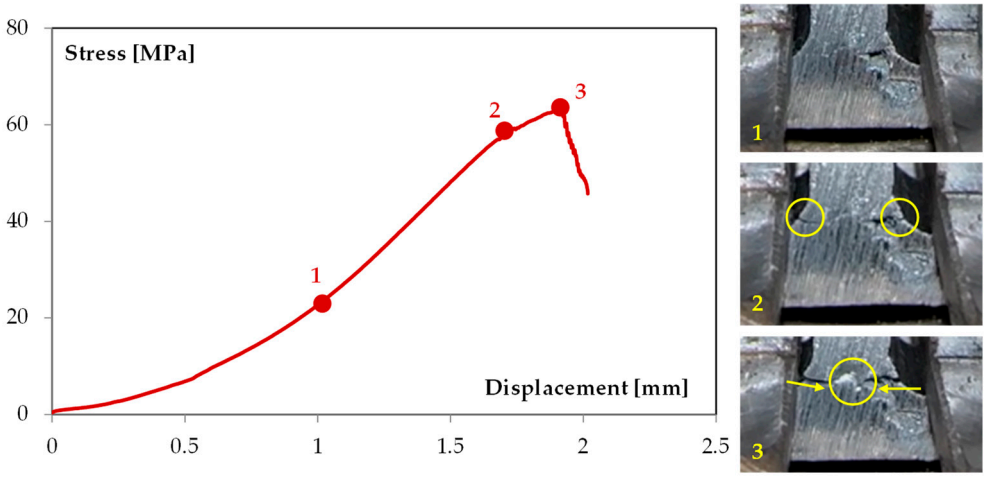

Figure 6. Typical stress-displacement curve for 500 rpm sample.

Particularly, it is possible to observe the following steps:

- Initial Loading Phase: At the onset, the curve exhibits a linear increase in load with displacement, indicating elastic deformation of the material. During this phase, the material responds proportionally to the applied load without permanent deformation;
- Onset of Plastic Deformation and Crack Initiation: As the load continues to increase, the curve begins to deviate from linearity, marking the transition to plastic deformation. At this stage, microstructural changes occur, leading to the initiation of cracks. The first accompanying image captures the sample during the initial stages of the test, prior to visible crack formation;
- Crack Propagation: With further loading, the curve approaches its peak, and the material undergoes significant plastic deformation. The second image illustrates the propagation of initial cracks, as denoted by the circles. This phase is characterized by the growth and coalescence of microvoids, leading to the advancement of cracks through the material. The material's ability to undergo plastic deformation allows for the redistribution of stress, delaying catastrophic failure;
- Peak Load and Onset of Final Fracture: The curve reaches its maximum load-bearing capacity at the peak, beyond which the load begins to decline. This decline signifies the material's reduced ability to withstand the applied load due to extensive internal damage. The third image captures the final ductile fracture occurring in the central region of the sample. This type of fracture is characterized by significant plastic deformation, often presenting as a cup-and-cone fracture surface, indicative of the material's ductile nature;
- Post-Fracture Behavior: Following the peak, the load decreases steadily as the material can no longer sustain the applied stress, leading to complete separation. The gradual slope of the descending curve reflects the material's capacity to absorb energy through plastic deformation before final failure, a desirable trait in applications requiring toughness and resistance to sudden fracture.

Then, this curve for the 500 rpm welded sample demonstrates a typical ductile fracture behavior, characterized by initial elastic deformation, followed by plastic deformation with crack initiation and propagation, culminating in a ductile fracture with significant energy absorption. This behavior suggests that the welding parameters at 500 rpm facilitated optimal material flow and bonding, resulting in a joint capable of sustaining substantial deformation before failure.

Figure 7 illustrates the load-displacement curve for the sample welded at 700 rpm, accompanied by sequential images depicting key stages in the fracture process.

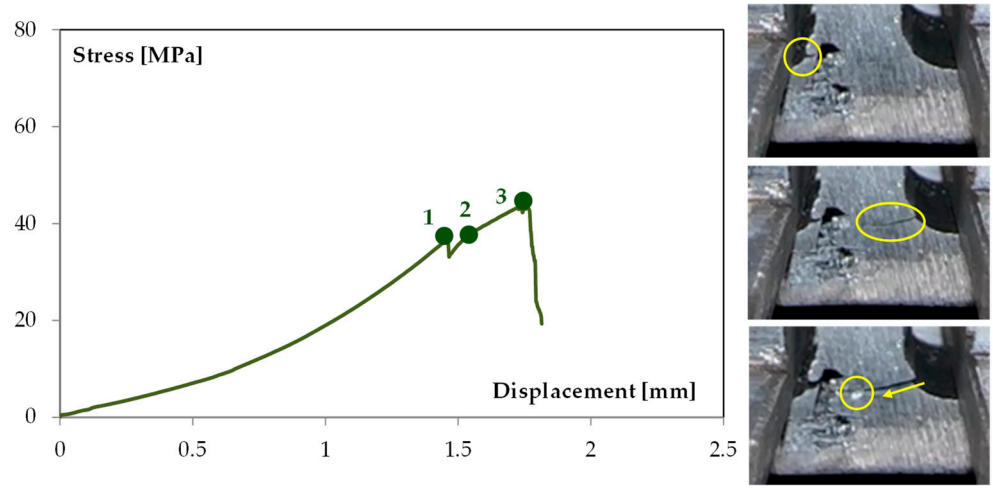

Figure 7. Typical stress-displacement curve for 700 rpm sample.

This representation provides insight into the material's behavior under load and highlights the influence of internal defects, particularly wormholes, on the fracture mechanism. Also in this case, it is possible to observe several steps:

- Initial Elastic Phase: The curve begins with a linear increase in load relative to displacement, indicating elastic deformation. During this phase, the material responds proportionally to the applied load without permanent deformation;
- First Peak and Wormhole Wall Fracture: As the load increases, the curve reaches an initial peak, corresponding to the fracture of the wormhole wall within the Weld Zone. This initial peak is absent in the 500 rpm sample, suggesting that higher rotational speeds may contribute to the formation of internal defects such as wormholes. The first image captures this stage, highlighting the initial crack formation at the wormhole site;
- Crack Propagation on Opposite Side: Following the initial peak, the load decreases slightly before increasing again, indicating the material's attempt to redistribute stress. During this phase, a crack initiates on the side opposite to the wormhole and begins to propagate. The second image illustrates this crack propagation, as denoted by the arrows. This behavior suggests that the presence of the wormhole creates stress concentrations, leading to crack initiation on the opposing side;
- Second Peak and Central Fracture: The curve reaches a second peak as the material's load-bearing capacity is temporarily restored. However, as the crack propagates towards the center, the load decreases sharply, culminating in a central fracture. The third image captures this final fracture, characterized by a brittle failure mode with minimal plastic deformation;
- Post-Fracture Behavior: After the central fracture, the load drops to zero, indicating complete separation of the material. The steep decline in the curve reflects the material inability to absorb energy through plastic deformation, a characteristic of brittle fracture.

The load-displacement curve for the 700 rpm welded sample exhibits a distinct initial peak corresponding to the fracture of internal defect structures, followed by crack initiation and propagation on the opposite side, leading to a central brittle fracture. This behavior contrasts with the ductile fracture observed in the 500 rpm sample and suggests that higher rotational speeds may introduce internal defects that compromise the joint's integrity. Although internal defects are also present in the 500 rpm sample, their influence is less pronounced, likely due to smaller size and reduced stress concentration effects, resulting in a more ductile fracture behavior. Fracture surface observations revealed the presence of weld imperfections, particularly wormholes, which were most prominent in joints fabricated at rotational speeds of 700 rpm and 900 rpm. These defects, likely caused by turbulent material flow and insufficient consolidation, acted as stress concentrators, contributing to

premature failure. In contrast, joints fabricated at 500 rpm exhibited significantly fewer and smaller imperfections, indicating more stable material mixing and a better thermal balance during welding. This correlation between defect formation and joint performance highlights the critical role of optimizing rotational speed to minimize imperfections and enhance joint quality. These findings underscore the importance of optimizing welding parameters to minimize defect formation and enhance joint performance [32]. The sample welded at 900 rpm exhibits a similar load-displacement behavior to the 700 rpm sample, as evidenced in Figure 8, indicating that higher rotational speeds may lead to comparable internal defects and fracture mechanisms.

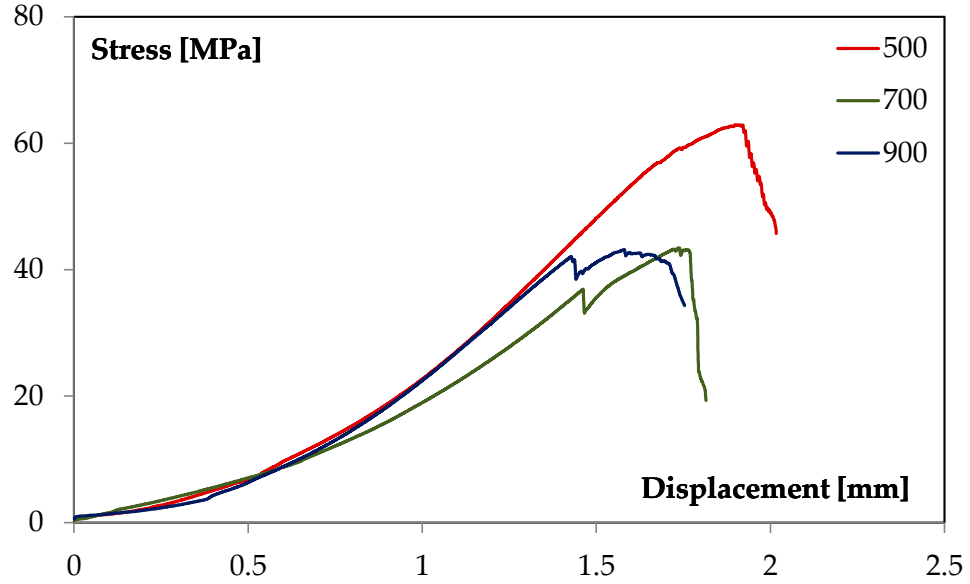

Figure 8. Comparison of stress-displacement curves.

The comparative analysis of joint strengths for samples welded at rotational speeds of 500, 700, and 900 rpm (Figure 9) reveals a notable dispersion in the data. Despite the scatter, the results indicate that joints welded at 500 rpm generally exhibit higher strength due to better material flow and fewer defects, such as wormholes. This highlights the critical influence of rotational speed on joint quality.

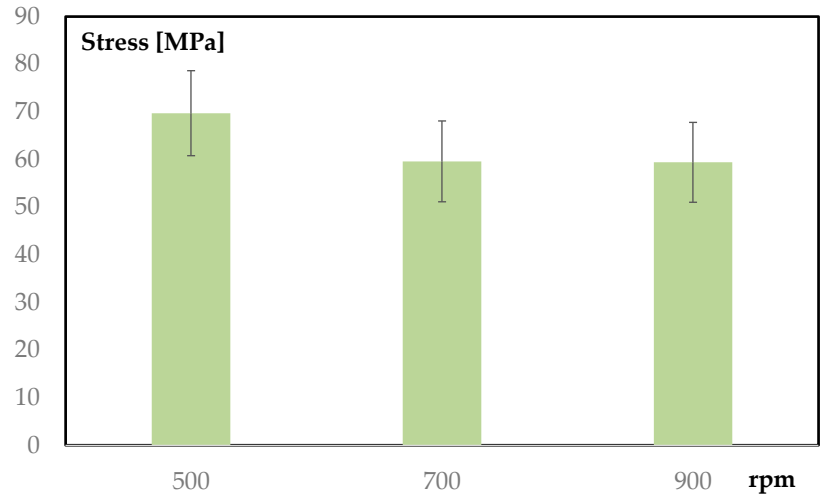

Figure 9. Comparison of pull-out resistance for all the three samples.

Lower rotational speeds generate less heat, promoting a more controlled material flow and reducing the likelihood of defect formation. This controlled environment facilitates

better consolidation of the material, resulting in joints with fewer internal voids and improved mechanical properties.

Conversely, higher rotational speeds (700 and 900 rpm) result in excessive heat generation, leading to turbulent material flow and an increased likelihood of internal defects, such as wormholes. The elevated temperatures also induce microstructural changes, such as grain coarsening, that adversely affect the joint's strength. These findings underline that rotational speed directly impacts the mechanical performance of welded joints. Specifically, the results demonstrate that 500 rpm provides a balance between heat input, material flow, and defect minimization, resulting in superior joint quality. This study offers actionable insights into the optimization of welding parameters to achieve high-quality joints for industrial applications.

In Figure 10, the observations of fracture surfaces in friction stir welded (FSW) samples at rotational speeds of 500, 700, and 900 rpm reveals notable differences in three key regions: the Stir Zone (a), the Wormhole Defect area (b), and the Transition Zone (c).

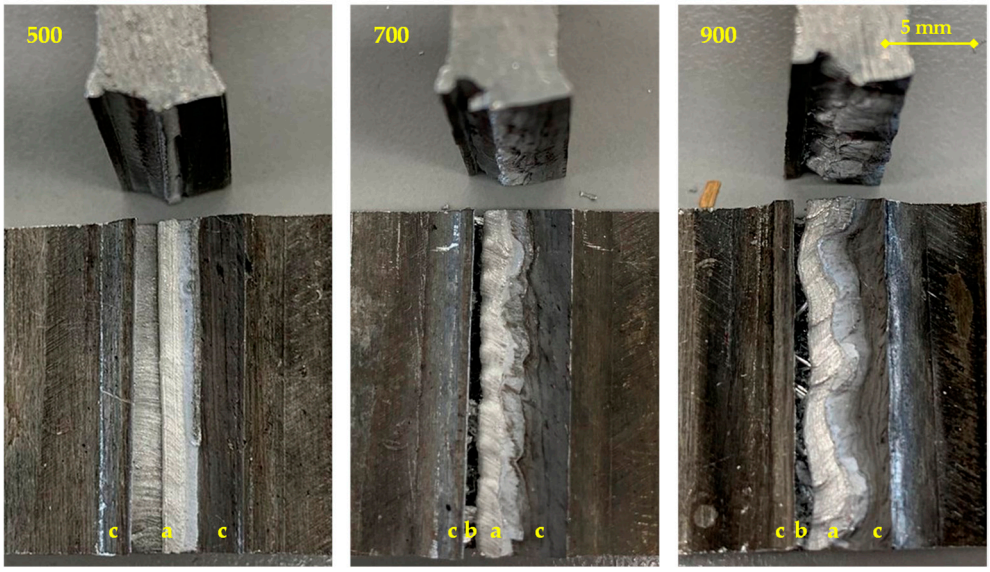

Figure 10. Failure surfaces.

At 500 rpm, the SZ exhibits a uniform and well-mixed appearance, indicating effective material stirring. In contrast, at 700 and 900 rpm, the SZ becomes less homogeneous, displaying signs of turbulence and irregular material flow. Regarding the Wormhole Defect area, while wormholes are present across all samples, their positioning differs. In the 500 rpm sample, the wormhole is situated in a manner that influences the fracture path differently compared to the 700 and 900 rpm samples. This positional variation affects how the wormhole impacts the mechanical integrity of the joint. The Transition Zone, which lies between the SZ and the base material, also varies with rotational speed. At 500 rpm, this zone appears more gradual, suggesting a smoother transition between stirred and unstirred material. In contrast, at 700 and 900 rpm, the Transition Zone becomes more pronounced, with sharper boundaries and thinner features, indicating a steeper gradient in thermal and mechanical effects.

In the 500 rpm sample, the Transition Zone (Region C) appears smoother and more gradual in its transition from the Stir Zone to the base material. This gradual shift suggests a more balanced thermal gradient and mechanical transition due to the controlled heat input at this lower rotational speed, which may contribute to a more stable microstructure and improved mechanical properties. In contrast, at higher rotational speeds (700 and 900 rpm), the Transition Zone shows sharper boundaries and thinner features, indicating a steeper gradient and increased stress, which could lead to residual stresses and reduced weld quality. These observations suggest that higher rotational speeds may lead to increased

heat input and turbulent material flow, resulting in more pronounced defects and transition zones. Conversely, a lower rotational speed appears to promote more stable material flow and fewer defects, leading to improved weld quality [33].

3.2. Micro-Hardness

The microhardness profiles along the skin direction for samples welded at rotational speeds of 500, 700, and 900 rpm exhibit distinct characteristics, reflecting the microstructural changes induced by each welding parameter, as illustrated in Figure 11 where each point represents the value of an individual indentation along the three measurement lines (upper, middle, lower).

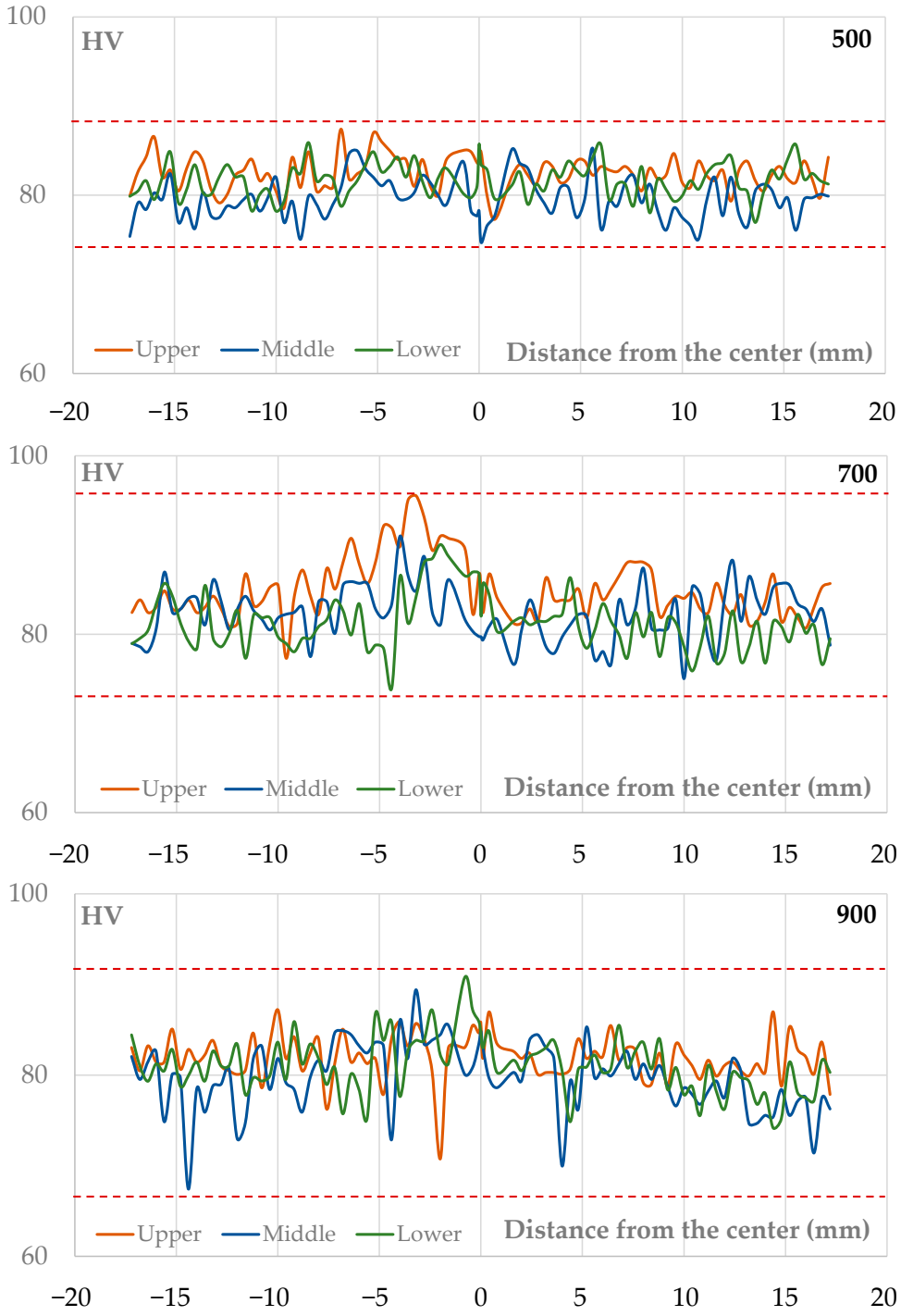

Figure 11. Micro-hardness measurements along the skin direction.

For the 500 rpm sample, the microhardness distribution is relatively uniform across the three measurement lines, with values ranging approximately between 75 HV and 90 HV, centering around 80 HV. This uniformity indicates a stable and homogeneous microstructure, suggesting that the heat input at this rotational speed is sufficient for effective material plasticization without causing overheating. Moderate heat input promotes the formation of a fine and consistent microstructure, as supported by studies on friction stir welding (FSW) of aluminum alloys [34].

For the 700 rpm sample, the microhardness profiles display more pronounced variations, with values oscillating between 70 HV and 100 HV. The three measurement lines show significant discrepancies, indicating a less uniform microstructure. The increased rotational speed leads to higher heat input, which can cause grain growth and uneven hardness distribution. This behavior aligns with findings in the literature, where excessive heat input during FSW results in undesirable microstructural changes [35].

For the 900 rpm sample, the profiles exhibit even more marked fluctuations, with hardness values ranging from 65 HV to 95 HV. The distinct separation among the three lines reflects significant heterogeneity in the microstructure. The elevated heat input at this rotational speed may lead to overheating, causing excessive grain growth and a reduction in hardness. Studies have shown that high heat input can negatively affect the microstructure and mechanical properties of welded joints [36].

The analysis of microhardness profiles highlights how rotational speed directly influences heat input and, consequently, the microstructure of the welded joint. A rotational speed of 500 rpm appears to offer an optimal balance, ensuring adequate heat input for effective plasticization without causing overheating. This results in a uniform microstructure and consistent hardness values, which are crucial for maintaining the mechanical integrity of the joint. In contrast, higher rotational speeds introduce variability in microstructure and hardness, potentially compromising the joint's performance.

The microhardness profiles along the skin direction for samples welded at rotational speeds of 500, 700, and 900 rpm allow us to define the approximate positions of the characteristic zones in friction stir welding (FSW). These zones include the Stir Zone (SZ), Thermo-Mechanically Affected Zone (TMAZ), Heat-Affected Zone (HAZ), and Base Metal (BM). Although hardness values fluctuate, the positions of these zones remain consistent and provide valuable insights into the effects of rotational speed on material behavior.

The approximate boundaries of the characteristic zones for each rotational speed were identified based on the microhardness profiles (see Table 3). For the 500 rpm sample, the Stir Zone (SZ) extends from approximately −5 mm to +5 mm around the weld center. This region corresponds to the area of intense plasticization and material mixing. The Thermo-Mechanically Affected Zone (TMAZ) lies between −10 mm and −5 mm, as well as +5 mm and +10 mm, representing a transitional area where thermal and mechanical effects are present but less intense than in the SZ. Beyond the TMAZ, the Heat-Affected Zone (HAZ) spans from −18 mm to −10 mm and +10 mm to +18 mm, where the material is affected by heat without undergoing significant plastic deformation. Outside these zones, the Base Metal (BM) remains unaffected by the welding process, extending beyond ±18 mm.

Table 3. The approximate boundaries of the characteristic zones for each rotational speed.

rpm	SZ	TMAZ	HAZ	BM
500	−5 mm to +5 mm	−10 mm to −5 mm +5 mm to +10 mm	−18 mm to −10 mm +10 mm to +18 mm	Beyond ±18 mm
700	−4 mm to +4 mm	−9 mm to −4 mm +4 mm to +9 mm	−15 mm to −9 mm +9 mm to +15 mm	Beyond ±15 mm
900	−3 mm to +3 mm	−8 mm to −3 mm +3 mm to +8 mm	−12 mm to −8 mm +8 mm to +12 mm	Beyond ±12 mm

At 700 rpm, the boundaries shift due to increased heat input. The SZ is centered between −4 mm and +4 mm, indicating the main region of material stirring and plasticization. The TMAZ extends from −9 mm to −4 mm and +4 mm to +9 mm, reflecting a transitional area influenced by both thermal and mechanical effects. The HAZ ranges from −15 mm to −9 mm and +9 mm to +15 mm, where thermal effects dominate without significant deformation. Beyond ±15 mm, the BM remains unaffected.

For the 900 rpm sample, the SZ is narrower, spanning from approximately −3 mm to +3 mm, corresponding to the region of highest heat input and material stirring. The TMAZ is located between −8 mm to −3 mm and +3 mm to +8 mm, where more pronounced thermal and mechanical effects are observed. The HAZ spans from −12 mm to −8 mm and +8 mm to +12 mm, reflecting significant thermal softening without substantial plastic deformation. The BM lies beyond ±12 mm, where the material retains its original properties.

This classification provides an approximate spatial definition of the different zones across the weld. The positioning of these zones is consistent with the expected effects of the FSW process. At lower rotational speeds (500 rpm), the SZ and TMAZ are broader, indicating controlled heat input and effective mixing. At higher speeds (700 and 900 rpm), the zones become narrower and exhibit more pronounced transitions, reflecting the challenges associated with increased heat input and material instability.

Figure 12 provides a clear comparison of the average microhardness values within the Stir Zone (SZ) for the three rotational speeds (500, 700, and 900 rpm) across the upper, middle, and lower measurement lines. This visualization highlights how the rotational speed influences the uniformity and consistency of the microstructure in the SZ.

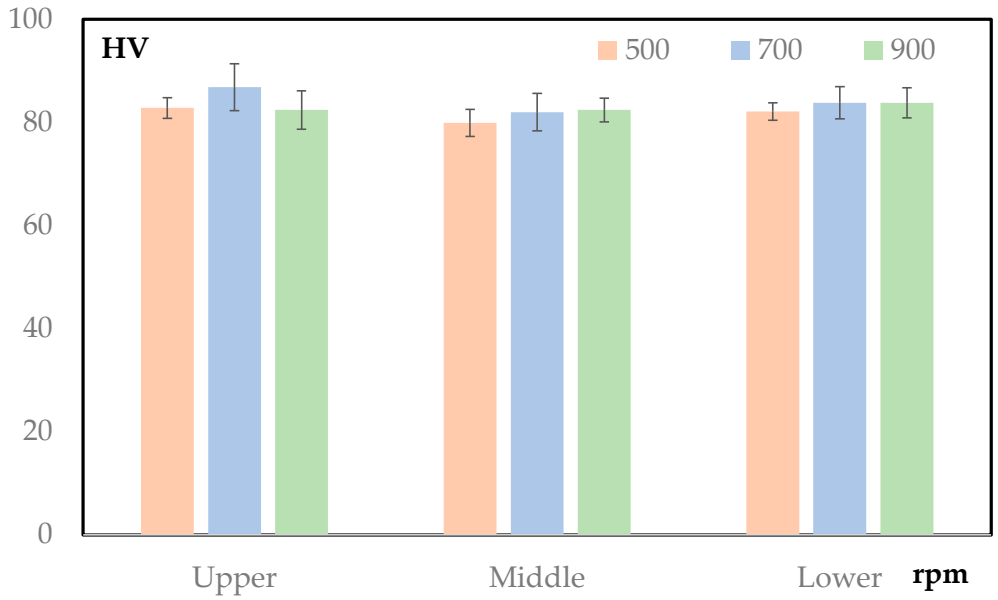

Figure 12. Comparison of micro-hardness measurements in the stir zone.

For the 500 rpm sample, the average hardness values across the upper, middle, and lower lines are closely aligned, with minimal variation and error bars. This uniformity confirms a stable and homogeneous microstructure in the SZ. The controlled heat input at 500 rpm ensures effective plasticization without overheating, leading to well-distributed mechanical properties throughout the SZ. For the 700 rpm sample, a slight increase in average hardness is observed compared to the 500 rpm sample, particularly for the upper and middle lines. However, the error bars suggest more variability in hardness among the three measurement lines. This indicates that while the material experiences higher heat input at this rotational speed, it may introduce microstructural inconsistencies and localized hardness fluctuations within the SZ. For the 900 rpm sample, the hardness values are comparable to the 700 rpm sample, but the error bars are slightly larger, reflecting increased variability. This suggests that the excessive heat input at 900 rpm disrupts the

uniform mixing of materials in the SZ. Overheating may result in grain coarsening and localized softening, leading to reduced microstructural stability.

Consequently, the 500 rpm sample demonstrates the most consistent hardness distribution, highlighting the importance of a moderate heat input to maintain a uniform microstructure. The 700 and 900 rpm samples show increased hardness variability, particularly in the upper and middle lines. This aligns with the earlier observations that higher rotational speeds introduce thermal gradients and turbulence in material flow, reducing the overall homogeneity of the SZ. This analysis reinforces the advantage of using a rotational speed of 500 rpm for achieving consistent and uniform mechanical properties in the Stir Zone. The gradual increase in variability at 700 and 900 rpm underscores the trade-off between higher process efficiency and the potential for reduced joint quality due to microstructural instability.

The microhardness profiles along the stringer direction, represented in Figure 13, illustrate the transition between the skin (AA6082) and stringer (AA5083) materials at the midpoint of the *x*-axis (0 mm). The presence of three distinct measurement lines (left, middle, right) provides a detailed view of the interface behavior under different rotational speeds.

For the 500 rpm sample, the transition from AA5083 to AA6082 exhibits a smooth and gradual increase in hardness across all three measurement lines, with values ranging from approximately 40 HV to 80 HV. This gradual transition is consistent across the left, middle, and right lines, indicating effective material mixing and a homogeneous interface. The moderate heat input at 500 rpm ensures controlled material flow, enabling a seamless blend between the skin and stringer materials. The consistent alignment of the three lines demonstrates excellent repeatability and stability, highlighting this rotational speed as optimal for minimizing stress concentrations and enhancing joint integrity.

For the 700 rpm sample, the transition becomes noticeably sharper compared to the 500 rpm sample. Hardness increases abruptly from approximately 40 HV to 80 HV near the boundary. The three measurement lines begin to diverge slightly, with the left and right lines showing more pronounced fluctuations compared to the middle line. This suggests uneven material mixing, potentially caused by the higher heat input disrupting the flow dynamics. The abrupt transition reflects limited intermixing between the skin and stringer materials, potentially leading to stress concentrations and reduced joint stability. This behavior may result in a less ductile and more brittle interface.

For the 900 rpm sample, the profiles at 900 rpm exhibit the most abrupt transition, with hardness values sharply increasing from 40 HV to 80 HV within a very narrow zone. Significant discrepancies between the left, middle, and right lines highlight inconsistent material behavior at this rotational speed. This irregularity is indicative of localized overheating and turbulent material flow, which inhibit effective inter-diffusion between AA6082 and AA5083. The distinct separation of the three curves suggests a lack of uniformity in the interface, likely resulting in higher stress concentrations and structural weaknesses in the joint.

The comparative analysis of the microhardness profiles underscores the critical role of rotational speed in determining the quality of the skin–stringer interface. The 500 rpm sample demonstrates superior material mixing and uniformity, resulting in a gradual transition and reduced stress concentrations. In contrast, the 700 and 900 rpm samples exhibit increasingly abrupt transitions and greater variability between the measurement lines, reflecting limited mixing and potential weaknesses at the boundary [37].

This behavior correlates strongly with the fracture surface conformations observed during mechanical testing. The smoother and more homogeneous hardness transition in the 500 rpm sample aligns with ductile fracture characteristics and enhanced joint toughness. Conversely, the sharper transitions and variability in hardness profiles for the 700 and 900 rpm samples are consistent with brittle fracture surfaces, characterized by localized stress concentrations and defects at the interface.

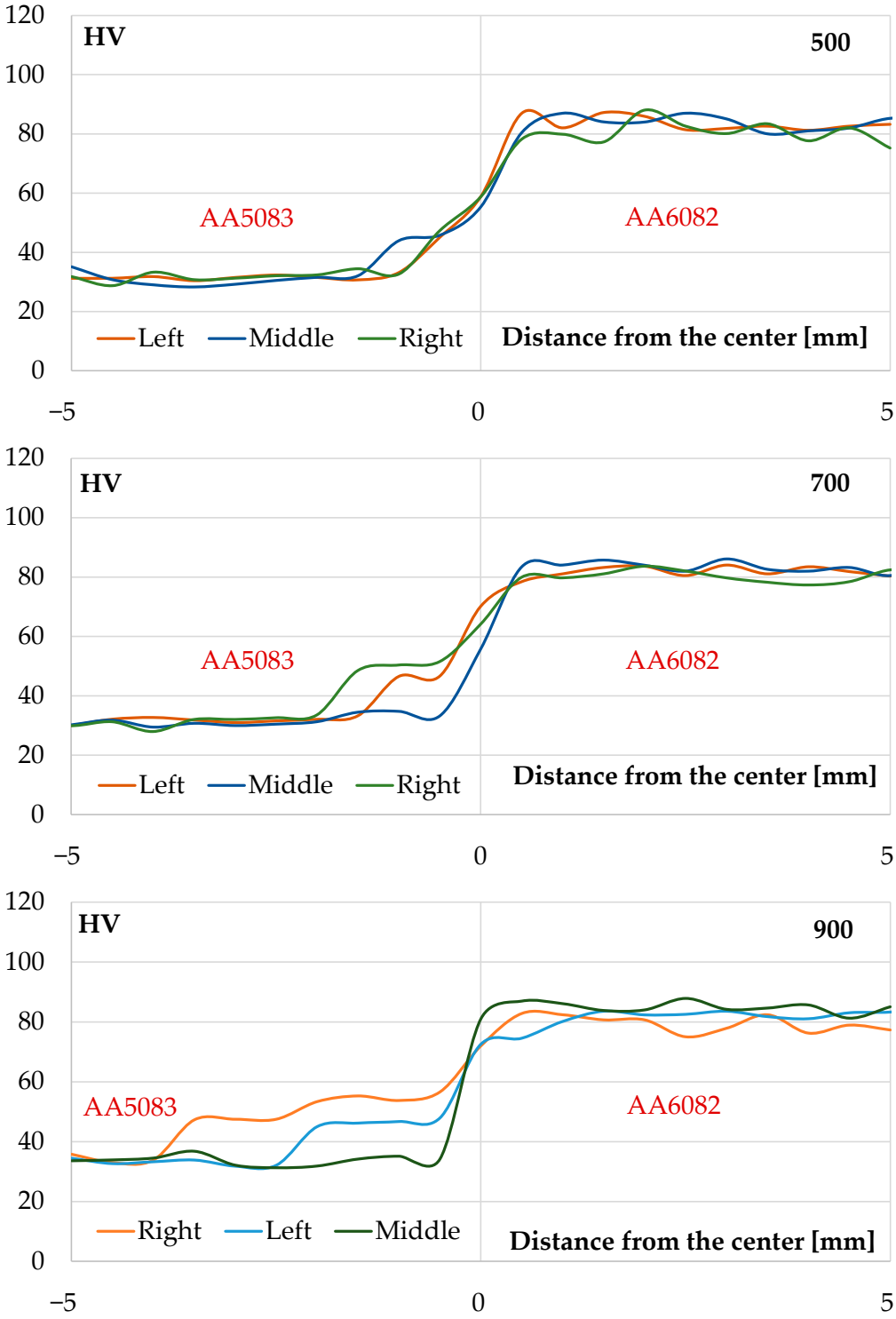

Figure 13. Micro-hardness measurements along the stringer direction.

4. Conclusions

This study investigates the influence of rotational speed on the mechanical and microstructural properties of friction stir welded T-joints made from AA5083 and AA6082 alloys. The results demonstrate that rotational speed significantly affects defect formation and joint performance.

Joints fabricated at 500 rpm exhibit higher mechanical strength and a more uniform microhardness profile, attributed to moderate heat input, which facilitates controlled material mixing and minimizes defect formation. In contrast, joints produced at 700 and

900 rpm show reduced mechanical performance and irregular hardness profiles due to increased heat input, leading to grain coarsening and the formation of defects such as wormholes. Fracture surface analysis confirms that these defects act as stress concentrators, significantly compromising joint integrity.

The correlation between welding parameters, defect formation, and mechanical properties underscores the critical role of optimizing rotational speed to balance heat input and material flow. Specifically, a rotational speed of 500 rpm achieves a favorable balance, resulting in fewer defects and improved joint performance. These findings provide valuable insights for the development of robust FSW joints, particularly for applications requiring lightweight and durable structures, such as in the marine industry.

Future research should explore additional process parameters, such as tool design and welding speed, to further enhance the quality of friction stir welded joints and minimize residual stresses associated with defect formation. Future research should focus on the impact properties of FSW T-joints, phase characterization in the weld zones, and the integration of AI-driven approaches for parameter optimization to further enhance joint quality and performance.

Author Contributions: Conceptualization, C.B. and G.B.; methodology, G.D.B., C.B. and G.B.; formal analysis, G.D.B., C.B., M.C. and D.C.; investigation, G.D.B., C.B., M.C. and D.C.; writing—original draft preparation, G.D.B., M.C. and D.C.; writing—review and editing, G.D.B., M.C. and D.C.; visualization, C.B. and G.B.; funding acquisition, G.D.B., C.B. and G.B. All authors have read and agreed to the published version of the manuscript.

Funding: This research was funded by the Sicilian Region on the European Regional Development Fund 2014–2020 as part of the project "Soluzioni Innovative per Mezzi navali ad Alto Risparmio Energetico (SI-MARE)", grant number 08ME7219090182.

Data Availability Statement: The original contributions presented in the study are included in the article; further inquiries can be directed to the corresponding author.

Conflicts of Interest: The authors declare no conflicts of interest.

References

1. Bharti, S.; Kumar, S.; Singh, I.; Kumar, D.; Bhurat, S.S.; Abdullah, M.R.; Rahimian Koloor, S.S. A Review of Recent Developments in Friction Stir Welding for Various Industrial Applications. *J. Mar. Sci. Eng.* **2023**, *12*, 71. [CrossRef]
2. Wang, G.-Q.; Zhao, Y.-H.; Tang, Y.-Y. Research Progress of Bobbin Tool Friction Stir Welding of Aluminum Alloys: A Review. *Acta Metall. Sin. (Engl. Lett.)* **2020**, *33*, 13–29. [CrossRef]
3. Manjhi, S.K.; Das, A.; Prasad, S.B. Review on Joining of Aluminum Alloy by Solid-State Welding Technique. *Mater. Today Proc.* **2020**, *26*, 1255–1261. [CrossRef]
4. Khedr, M.; Hamada, A.; Järvenpää, A.; Elkatatny, S.; Abd-Elaziem, W. Review on the Solid-State Welding of Steels: Diffusion Bonding and Friction Stir Welding Processes. *Metals* **2022**, *13*, 54. [CrossRef]
5. Richter-Trummer, V.; Suzano, E.; Beltrão, M.; Roos, A.; dos Santos, J.F.; de Castro, P.M.S.T. Influence of the FSW Clamping Force on the Final Distortion and Residual Stress Field. *Mater. Sci. Eng. A* **2012**, *538*, 81–88. [CrossRef]
6. Gunasekaran, R.; Gobinath, V.K.; Suganeswaran, K.; Nithyavathy, N.; Arun Kumar, S. Applications of Friction Stir Welding. In *Friction Stir Welding and Processing*; Wiley: Hoboken, NJ, USA, 2024; pp. 245–258.
7. Di Bella, G.; Borsellino, C.; Buffa, G.; Simoncini, M.; Forcellese, A.; Panfiglio, S. *White Paper on Innovative Joining Technologies for Naval Applications*; Springer Nature: Cham, Switzerland, 2024; pp. 275–294.
8. Pratap Kumar, J.; Raj, A.; Arul, K.; Mohanavel, V. A Literature Review on Friction Stir Welding of Dissimilar Materials. *Mater. Today Proc.* **2021**, *47*, 286–291. [CrossRef]
9. Patel, V.; Li, W.; Wang, G.; Wang, F.; Vairis, A.; Niu, P. Friction Stir Welding of Dissimilar Aluminum Alloy Combinations: State-of-the-Art. *Metals* **2019**, *9*, 270. [CrossRef]
10. Yang, Y.; Luo, Z.; Zhang, Y.; Su, J. Dissimilar Welding of Aluminium to Steel: A Review. *J. Manuf. Process* **2024**, *110*, 376–397. [CrossRef]
11. Patel, M.M.; Badheka, V.J. A Review on Friction Stir Welding (FSW) Process for Dissimilar Aluminium to Steel Metal Systems. *Weld. Int.* **2024**, *38*, 91–115. [CrossRef]
12. Ezuber, H.; El-Houd, A.; El-Shawesh, F. A Study on the Corrosion Behavior of Aluminum Alloys in Seawater. *Mater. Des.* **2008**, *29*, 801–805. [CrossRef]
13. Wahid, M.A.; Siddiquee, A.N.; Khan, Z.A. Aluminum Alloys in Marine Construction: Characteristics, Application, and Problems from a Fabrication Viewpoint. *Mar. Syst. Ocean Technol.* **2020**, *15*, 70–80. [CrossRef]

14. Rudrapati, R. Recent Advances in Joining of Aluminum Alloys by Using Friction Stir Welding. In *Mass Production Processes*; IntechOpen: London, UK, 2020.
15. Nor, A.M.Y.; Shazarel, S. Friction Stir Welding of Dissimilar Aluminium Alloys for Marine Applications. *Res. Prog. Mech. Manuf. Eng.* **2024**, *5*, 304–317.
16. Osorio Díaz, M.A.; Franco Arenas, F.; Unfried-Silgado, J. Effects of Process Parameters on Mechanical Properties and Microstructure of AA6063-T6 and AA5052-H32 Dissimilar Friction Stir Welded Joints. *Soldag. Inspeção* **2024**, *29*, e2911. [CrossRef]
17. Verma, S.; Kumar, V. Optimization of Friction Stir Welding Parameters of Dissimilar Aluminium Alloys 6061 and 5083 by Using Response Surface Methodology. *Proc. Inst. Mech. Eng. C J. Mech. Eng. Sci.* **2021**, *235*, 7009–7020. [CrossRef]
18. Fratini, L.; Micari, F.; Squillace, A.; Giorleo, G. Experimental Characterization of FSW T-Joints of Light Alloys. *Key Eng. Mater.* **2007**, *344*, 751–758. [CrossRef]
19. Tavares, S.M.O.; Castro, R.A.S.; Richter-Trummer, V.; Vilaça, P.; Moreira, P.M.G.P.; de Castro, P.M.S.T. Friction Stir Welding of T-Joints with Dissimilar Aluminium Alloys: Mechanical Joint Characterisation. *Sci. Technol. Weld. Join.* **2010**, *15*, 312–318. [CrossRef]
20. Jesus, J.S.; Costa, J.M.; Loureiro, A.; Ferreira, J.M. Assessment of Friction Stir Welding Aluminium T-Joints. *J. Mater. Process Technol.* **2018**, *255*, 387–399. [CrossRef]
21. Sabry, I.; El-Kassas, A.M.; Mourad, A.-H.I.; Thekkuden, D.T.; Abu Qudeiri, J. Friction Stir Welding of T-Joints: Experimental and Statistical Analysis. *J. Manuf. Mater. Process.* **2019**, *3*, 38. [CrossRef]
22. Rana, H.; Buffa, G.; Micari, F.; Fratini, L. *Numerical Investigation on Dissimilar Titanium-Aluminum T-Joints Produced by Friction Stir Welding: Process Mechanics and Material Flow*; Springer Nature: Cham, Switzerland, 2024; pp. 157–168.
23. Memon, S.; Murillo-Marrodán, A.; Lankarani, H.M.; Aghajani Derazkola, H. Analysis of Friction Stir Welding Tool Offset on the Bonding and Properties of Al–Mg–Si Alloy T-Joints. *Materials* **2021**, *14*, 3604. [CrossRef]
24. Salloomi, K.N. Fully Coupled Thermomechanical Simulation of Friction Stir Welding of Aluminum 6061-T6 Alloy T-Joint. *J. Manuf. Process.* **2019**, *45*, 746–754. [CrossRef]
25. Silva, A.C.F.; Braga, D.F.O.; Figueiredo, M.A.V.D.; Moreira, P.M.G.P. Friction Stir Welded T-Joints Optimization. *Mater. Des.* **2014**, *55*, 120–127. [CrossRef]
26. Di Bella, G.; Favaloro, F.; Borsellino, C. Effect of Process Parameters on Friction Stir Welded Joints between Dissimilar Aluminum Alloys: A Review. *Metals* **2023**, *13*, 1176. [CrossRef]
27. Peel, M.J.; Steuwer, A.; Withers, P.J.; Dickerson, T.; Shi, Q.; Shercliff, H. Dissimilar Friction Stir Welds in AA5083–AA6082. Part I: Process Parameter Effects on Thermal History and Weld Properties. *Metall. Mater. Trans. A* **2006**, *37*, 2183–2193. [CrossRef]
28. Steuwer, A.; Peel, M.J.; Withers, P.J. Dissimilar Friction Stir Welds in AA5083–AA6082: The Effect of Process Parameters on Residual Stress. *Mater. Sci. Eng. A* **2006**, *441*, 187–196. [CrossRef]
29. Acerra, F.; Buffa, G.; Fratini, L.; Troiano, G. On the FSW of AA2024-T4 and AA7075-T6 T-Joints: An Industrial Case Study. *Int. J. Adv. Manuf. Technol.* **2010**, *48*, 1149–1157. [CrossRef]
30. *ASTM E384-17*; Standard Test Method for Microindentation Hardness of Materials. ASTM: West Conshohocken, PA, USA, 2017.
31. Jacquin, D.; Guillemot, G. A Review of Microstructural Changes Occurring during FSW in Aluminium Alloys and Their Modelling. *J. Mater. Process Technol.* **2021**, *288*, 116706. [CrossRef]
32. Ajri, A.; Rohatgi, N.; Shin, Y.C. Analysis of Defect Formation Mechanisms and Their Effects on Weld Strength during Friction Stir Welding of Al 6061-T6 via Experiments and Finite Element Modeling. *Int. J. Adv. Manuf. Technol.* **2020**, *107*, 4621–4635. [CrossRef]
33. Jamshidi Aval, H.; Galvão, I. Effect of Tool Rotational Speed on Microstructure and Mechanical Properties of Friction Stir Welded Al–16Si–4Cu–10SiC Composite/Al–4Cu–Mg Alloy Joints. *Metallogr. Microstruct. Anal.* **2024**, *13*, 504–518. [CrossRef]
34. Li, W.; Luo, Z.; Sun, Y.; Liu, X. Effect of Tool Speed on Microstructure Evolution and Mechanical Properties of Friction Stir Welded Joints of Al-Mg-Si Alloy with High Cu Content. *Metals* **2024**, *14*, 758. [CrossRef]
35. Nan, X.; Zhao, H.; Jia, B.-B.; Ma, C.; Sun, G.; Zhou, L.; Wang, R.; Song, X. The Effect of Rotational Speed on Microstructure and Mechanical Properties of Al/Ti Dissimilar Joint Produced by Refill Friction Stir Spot Welding. *J. Mater. Eng. Perform.* **2024**, 1–13. [CrossRef]
36. Hu, Y.; Wang, Z.; Tao, T.; Chen, S.; Cui, H. Effect of Various Rotational Speeds on the Inhomogeneous Distribution of Microstructure and Toughness in Friction Stir Weld Joint of Q1100 Ultra-High Strength Steel. *Weld. World* **2024**, *68*, 2071–2081. [CrossRef]
37. Jain, S.; Mishra, R.S.; Mehdi, H. Influence of SiC Microparticles and Multi-Pass FSW on Weld Quality of the AA6082 and AA5083 Dissimilar Joints. *Silicon* **2023**, *15*, 6185–6197. [CrossRef]